Environmental Science: Atmospheres

ROYAL SOCIETY OF CHEMISTRY

PAPER

View Article Online
View Journal | View Issue

Cite this: *Environ. Sci.: Atmos.*, 2024, **4**, 252

Improving model representation of rapid ozone deposition over soil in the central Tibetan Plateau†

Chong Zhang,[a] Jianshu Wang,[a] Yingjie Zhang,[‡a] Wanyun Xu,[b] Gen Zhang,[b] Guofang Miao,[c] Jiacheng Zhou,[d] Hui Yu,[d] Weixiong Zhao,[d] Weili Lin,[e] Ling Kang,[a] Xuhui Cai,[a] Hongsheng Zhang[f] and Chunxiang Ye *[a]

Ozone soil deposition contributes a major part to the total deposition of ozone on land covered by low vegetation and perturbs the ozone budget on both regional and global scales. Large model-observation divergences in ozone soil deposition require continuous efforts to improve the mechanical understanding and model representation. Observation of ozone deposition over bare soil directly meets the requirement. Here, we performed field observation of ozone deposition over bare soil first available in the Tibetan Plateau (TP) using the aerodynamic gradient method. A top ozone deposition velocity with a daily mean of 0.49 ± 0.11 (1 sd) cm s^{-1} (1 May to 10 July 2019) and an hourly mean maximum across the diel pattern of 0.73 ± 0.67 cm s^{-1} in the afternoon were recorded. Such rapid ozone deposition was mainly attributed to extremely low soil resistance (R_{soil}), which was further regulated by median low soil clay content, dry conditions, and strong solar radiation in the central TP. Parameterization of R_{soil} in the newly developed Stella scheme was demonstrated to be effective according to our verification. An updated scheme was further attained with the inclusion of our observation and better represents the R_{soil} variability than the Stella scheme. More verification is therefore encouraged and hopefully to improve the Stella scheme. Finally, both the Stella scheme and our updated scheme showed great advantages over the oversimplified scheme in current models and should be considered more seriously for the sake of better representation of ozone soil deposition and its variability.

Received 25th October 2023
Accepted 30th December 2023

DOI: 10.1039/d3ea00153a

rsc.li/esatmospheres

Environmental significance

Tropospheric ozone is an important gaseous pollutant and a short-lived climate forcer that affects air quality, human health and climate. Ozone soil deposition represents a non-negligible fraction of ozone budget. However, it is highly underestimated by current models and therefore leads to ill-representation of ozone distribution. To explore the soil deposition mechanism and improve the model representation, we performed direct measurements of ozone deposition velocity on bare soil in the central Tibetan Plateau (TP), an ideal experimental field for its pristine nature in terms of weak human perturbation on both land use and ozone photochemistry. For the first time, our measurement recorded in the TP the top ozone deposition velocity on soil, which could be accounted for by measured meteorological and edaphic parameters. An updated parameterization scheme based on Stella *et al.* was summarized and better represented ozone deposition velocity and its environmental variability, relative to the schemes commonly used in chemical transport models. The Stella scheme is therefore worthy of more serious consideration for the sake of better representation of ozone soil deposition and its variability. Our data has also confirmed that ozone soil deposition in the TP is underestimated by current model evaluations.

[a]*SKL-ESPC & SEPKL-AERM, College of Environmental Sciences and Engineering and Center for Environment and Science, Peking University, Beijing, China. E-mail: c.ye@pku.edu.cn*

[b]*State Key Laboratory of Severe Weather & Key Laboratory for Atmospheric Chemistry of CMA, Institute of Atmospheric Composition, Chinese Academy of Meteorological Sciences, Beijing, China*

[c]*School of Geographical Sciences, Fujian Normal University, Fuzhou, China*

[d]*Laboratory of Atmospheric Physico-Chemistry, Anhui Institute of Optics and Fine Mechanisms, Chinese Academy of Science, Hefei, Anhui, China*

[e]*College of Life and Environmental Sciences, Minzu University of China, Beijing, China*

[f]*Department of Atmospheric and Oceanic Sciences, School of Physics, Peking University, Beijing, China*

† Electronic supplementary information (ESI) available. See DOI: https://doi.org/10.1039/d3ea00153a

‡ School of Ecology and Nature Conservation, Beijing Forestry University, Beijing, China.

1 Introduction

Tropospheric ozone is an important gaseous pollutant and a short-lived climate forcer that plays a key role in atmospheric oxidative capacity, oxidative damage to humans and vegetation, and climate change.[1–4] Obtaining accurate temporal and spatial variability of ozone is essential for assessing its role. While dense ozone measurement networks have been established in the United States, Europe, and eastern Asia, and great progress has been made in China in recent years, observational constraints on ozone are still absent in other regions, especially in background areas globally.[5] Chemical transport models (CTMs) are alternative tools to evaluate the temporal–spatial

variability in ozone in those regions where measurement is absent. Simulations of ozone by CTMs are numerical approximations of the budgets of ozone, including chemical reactions that lead to ozone formation and destruction, tropospheric influx from stratosphere–troposphere exchange, deposition loss, and convectional and advectional transport. However, the simulation representations are limited by our current incomplete understanding of and parameterization methods for these budget items.[6]

Simulation representation of tropospheric ozone, especially ozone at the surface, is sensitive to the representation of ozone dry deposition.[7–11] The resistance-analogy parameterization framework for ozone deposition developed by Wesely,[12] is widely accepted by different deposition schemes to explain and parameterize ozone deposition on various land cover types.[13–18] Briefly, the resistance analogy framework conceptualized the dry deposition of ozone or other pollutants as a three-step process including (1) ozone transport downward to a given surface by atmospheric turbulence, (2) mass transfer through the quasi-laminar sublayer around the interface of air and the surface, and (3) uptake on the surface. The ozone deposition velocity, v_d, can be expressed as the reciprocal of the total mass transfer resistance of these three-step processes, namely, aerodynamic resistance R_a, quasi-laminar sublayer resistance R_b, and surface resistance R_c.[12]

Studies comparing different deposition schemes at site-specific sites illustrate that the representation of R_c and its variability cause the largest differences of v_d.[19,20] Among different deposition schemes, R_a is typically modelled with different empirical formulae of the Monin–Obukhov similarity theory (MOST), and R_b is modelled with a same formula. Wu *et al.*[19] compared $R_a + R_b$ over a forest modelled by four different MOST-based models and found similar results. Combined with the relatively smaller contribution of $R_a + R_b$ than R_c to the total resistance (see Section 3.2 below), more attention is focused on the parameterization of R_c. The parameterization of R_c used in the resistance analogy considers the resistance of ozone uptake by stomatal, cuticular, and ground surfaces, the last of which mainly refers to soil surfaces. Relatively intensive field observations of ozone deposition have been performed over developed canopies.[21–28] Canopy related stomatal and cuticular uptake are the main ozone deposition paths in these observations. However, studies on crops found that the determining role of stomatal and cuticular resistances highly depends on canopy development and abundance.[29,30] On surfaces with lower and sparser canopies, such as growing croplands and grasslands, soil resistance (R_{soil}) could contribute up to 55% to total ozone deposition resistance; thus, v_d is more sensitive to R_{soil} for these land cover types.[31,32]

Ozone soil deposition contributes heavily to the global budget of ozone deposition because a considerable fraction of global land cover is desert, bare soil, and sparse vegetation. However, the modeling of ozone soil deposition remains highly uncertain. Gross model underestimation of ozone deposition on bare soil (equivalent to ozone soil deposition) was consistently found.[33,34] The large discrepancy of ozone soil deposition and its variability between measurements and simulations implies the poor representations of ozone soil deposition by current CTMs. The poor representation is mainly attributed to the oversimplified R_{soil} parameterization scheme that uses two-level prescribed values for dry and wet surfaces without more complex response relationships with soil moisture, soil temperature or soil clay content.[19] Modification attempts have been made with the aim of enabling model power to better describe the variability in R_{soil}. Either a positive dependence of R_{soil} on soil moisture or a negative dependence on temperature was reported based on site-specific observations, but the expressions between R_{soil} and moisture or temperature should not be extrapolated to other sites.[35–37] A few studies introduced a universal corrected function of soil moisture or temperature based on mathematical assumptions; however, field observation validation is rare.[7,38] Stella *et al.*[33,34] summarized their six field observations over bare soil and proposed a dual-parameter semiempirical R_{soil} parameterization (known as the "Stella scheme") involving soil clay content and surface relative humidity (RH_{surf}). In the Stella scheme, RH_{surf} is believed to better represent the varied and complex effect of meteorological parameters, such as surface temperature (T_{surf}), soil moisture, and solar radiation. Soil clay content, as a second influencing factor, reasonably accounts for the spatial heterogeneity of soil uptake reactivity toward ozone and therefore R_{soil}.

Although the Stella scheme seems to have the potential to describe R_{soil} and its variability, limited field observational validation hinders direct extrapolation or CTMs inclusion. The observations of ozone soil deposition were mostly conducted over agricultural fields after harvest to avoid interference of the canopy.[33] However, frequent agricultural activities, such as plowing, fertilization, and irrigation, can cause transformations in surface soil physics and chemical characteristics and potentially soil uptake reactivity toward ozone. Additionally, strong NO_x and/or VOCs emissions from agricultural soil can participate in the fast atmospheric chemical conversion of ozone and therefore significantly interfere with the measurement of ozone soil deposition.[42,43] Field observation of ozone deposition in environments with negligible NO or highly reactive VOCs sources is ideal in terms of less chemistry interference and human activity perturbation of soil but is sporadically available.[33] In addition, R_{soil} is highly affected by soil clay contents and hydrothermal conditions based on the previous summary, which are spatially heterogeneous in different climate regions. Previous observations were performed mostly in subtropical climate regions. Field observations in more climate regions are therefore highly demanded (Fig. 1). The TP is a typical highland climate region where both soil clay content and moisture are expected to be different from the subtropical climate regions. And TP is characterized as a highly pristine area and covered with sparse and low vegetation, implying weak perturbation of land use and ozone chemistry on ozone soil deposition.

The @Tibet series field campaign supports ozone deposition measurement over the Tibetan Plateau (TP). In this study, we took advantage of the ideal experimental field and performed the first measurement of ozone deposition velocity on bare soil in the TP, acquired from the aerodynamic gradient method. The

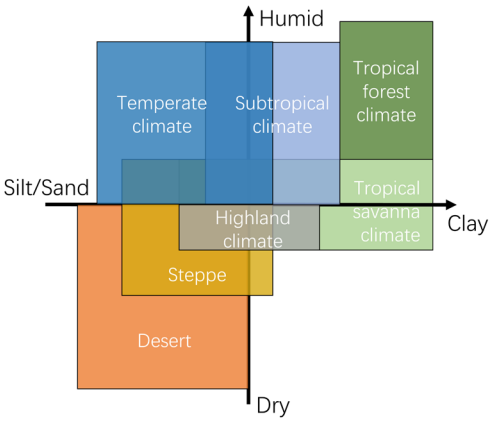

Fig. 1 Simplified concept of climatic regions with different soil clay contents and hydrothermal conditions. Previous measurements of soil resistance (R_{soil}) have been conducted mostly in subtropical climate regions in the figure. Data of climate classification is from Chen *et al.*[39] Soil clay content data is from Harmonized World Soil Database v2.0.[40] Humidity data is referenced to Kummu *et al.*[41]

aims of this study are (i) to measure v_d in the TP and to identify the factors controlling v_d and R_{soil} and (ii) to evaluate and improve the Stella scheme by inclusion of our verifications.

2 Methods

2.1 Measurements

The field measurement of ozone deposition was performed from 1 May to 10 July 2019 at Nam Co Comprehensive Observation and Research Station, Chinese Academy of Sciences (CAS) (NMC site, 30°46.30′N, 90°59.31′E, 4730 m a.s.l.), as an essential part of the @Tibet 2019 campaign. Due to power outages, instrument malfunctions and other factors, the valid data cover 50 days. Detailed descriptions of NMC site and @Tibet 2019 campaign can be found in previous studies.[44–46] NMC site is located in an open flat field ~1 km southeast of Nam Co Lake and more than 15 km to the north and west of the Nyainqêntanglha Mountains. In addition, a sublake of Nam Co Lake is ~280 m away from the site. NMC site is characterized by a continental background of the atmosphere with few surrounding populations, and isolated from Lhasa, the largest city in the TP.

High-altitude and mountainous environment results in a typical arctic–highland climate of this area. The monthly mean air temperature ranges from −7.8 °C to 12.2 °C, and solar radiation reaches 1200 W m^{-2} in May.[47] Annual precipitation of approximately 400 mm is concentrated during the Asian Summer Monsoon (ASM) period from June to September.[48] In this cold and arid area, the soil is poorly developed because of sporadic vegetation coverage and weak chemical weathering, which is embodied in a loose soil structure and low clay content.[49]

Air temperature and relative humidity (HMP155A, Vaisala, FI) and wind speed (010C, Met One, USA) profiles were measured at 1.8, 3.8, and 5.8 m height, and wind direction (020C, Met One, USA) was measured at 5.8 m. Solar radiation, including incoming and reflected shortwave and longwave radiation (CNR4, Kipp & Zonen, NL) and j(NO_2) (ultrafast CCD-detector spectrometer, Metcon, GER), were measured. Soil temperature and soil water content (CS655, Campbell Scientific Inc., USA) profiles were also measured at 5, 15, and 25 cm below ground. NO_2 concentration was measured by a sensitive incoherent broadband cavity enhanced absorption spectroscopy NO_2 analyzer.[50] As the NO concentration was too low to be measured, photostationary state calculation of the NO concentration (NO_PSS) was carried out with measured O_3, NO_2, and $j(NO_2)$.

Ozone flux was measured using the aerodynamic gradient (AG) method, with characterization of the micrometeorological environment by the eddy covariance (EC). The AG method is based on *K*-theory, an application of MOST. Similar to Fick's Law, the *K*-theory assumes that the turbulence flux can be expressed as the product of the turbulence exchange coefficient *K* and vertical concentration gradient. Therefore, the ozone flux can be calculated as follows:

$$F = -K\frac{\mathrm{d}[O_3]}{\mathrm{d}Z} \quad (1)$$

where *F* is the ozone flux (ppbv m s^{-1} or nmol m^{-2} s^{-1}), *K* is the turbulence exchange coefficient (m^2 s^{-1}), and $\frac{\mathrm{d}[O_3]}{\mathrm{d}Z}$ is the vertical ozone gradient between the two measurement heights (ppbv m^{-1} or nmol m^{-2}). A UV photometric ozone analyzer (Model 49i, Thermo-Environmental Instruments Inc., USA) measured the ozone concentration. Air was sampled at 6.8 m and 1.8 m of the tower through a 27 m Teflon sampling tube with sequential sampling in a 30 min duty cycle. A solenoid valve was used to control the measurement time of 15 min at each height. The measurement gap of 15 min at each height was filled by linear interpolation of adjacent data at the same height. Therefore, continuous ozone gradient was obtained. The sampling tube was covered by black foam for heat preservation and light shading. *K* is calculated as follows:[51]

$$K = \kappa u_*(z_2 - z_1)\left[\ln\frac{z_2 - d}{z_1 - d} - \psi_h\left(\frac{z_2 - d}{L}\right) + \psi_h\left(\frac{z_1 - d}{L}\right)\right] \quad (2)$$

where κ is von Karman's constant (0.4), u_* is the friction velocity (m s^{-1}), z_1 and z_2 are the lower and greater heights of ozone measurement respectively (m), *d* is the zero-plane displacement height (m), *L* is the Obukhov length (m), and $\psi_h(z/L)$ is the integrated stability correction function for heat:

$$\psi_h(z/L) = \begin{cases} 2\ln\left(\frac{1+y}{2}\right), & z/L < 0 \\ -5z/L, & z/L > 0 \end{cases} \quad (3)$$

where $y = (1 - 16z/L)^{1/2}$. As EC is a reliable method to characterize atmospheric turbulence, u_* and L were provided by the EC method and used in the AG method. The EC method was also used to measure fluxes of momentum, sensible heat (*H*), latent heat (LE), water vapor, and CO_2. The EC system includes an integrated CO_2/H_2O open-path gas analyzer and 3D sonic anemometer (IRGASON, Campbell Scientific Inc., USA), electronics for synchronizing gas and wind data (EC100, including

a temperature thermistor probe and a barometer, Campbell Scientific Inc., USA), and a data logger (CR3000, Campbell Scientific Inc., USA). The IRGASON was mounted at 6.8 m. Data were sampled and recorded at 10 Hz and processed by EddyPro software (version 7.0.8, LiCor, USA) for a 30 min flux averaging interval. Standard data processing methods were used, including spike removal, double axis rotation, linear detrending, humidity correction of sonic temperature, WPL correction and spectral correction.[52] Quality checks of raw data and flux results were also performed. The footprint was estimated by the Kljun *et al.*[53] method.

Ozone deposition velocity can be determined as follows:

$$v_d = -\frac{F}{[O_3]} \times 100 \quad (4)$$

where v_d is the ozone deposition velocity (cm s^{-1}), and $[O_3]$ is the average concentration of ozone between two measurement heights (ppbv).

2.2 Resistance analogy

The resistance analogy method describes the mechanism and kinetics of ozone deposition. It also provides a numerical model representation of v_d. By considering that the reciprocal of v_d is the total resistance to mass transfer, the influence of the above mentioned three processes on v_d can be expressed in terms of the following electrical analogy:

$$v_d = \frac{1}{R_{all}} = \frac{1}{R_a + R_b + R_c} \quad (5)$$

R_c consists of the resistances of these different surfaces, such as soil, leaf cuticular or ice. As the surface at the study area of NMC site is bare soil, R_c in this study is equal to the soil resistance R_{soil}. R_a and R_b are calculated as follows:

$$R_a(z) = (\kappa u_*)^{-1}\left[\ln\frac{z}{z_0} - \psi_h(z/L) + \psi_h(z_0/L)\right] \quad (6)$$

$$R_b(O_3) = 2(\kappa u_*)^{-1}(S_c/P_r)^{2/3} \quad (7)$$

where z is the reference height (mean ozone measurement height, m), z_0 is the roughness length for momentum (m), S_c is the Schmidt number, and P_r is the Prandtl number for air (0.72).

2.3 Calculation of surface parameters

Temperature and moisture at the surface, T_{surf} and RH_{surf}, instead of atmospheric or edaphic parameters, are recommended as measures of temperature and moisture conditions of soil uptake of ozone by Stella *et al.*[34] and have shown less variability than other measures. Thus, the same scheme is used in this study following the calculation method in Stella *et al.*:[32]

$$T_{surf} = \frac{H(R_a(z) + R_b)}{\rho C_p} + T_a \quad (8)$$

$$\chi_{H_2O,\,surf} = E(R_a(z) + R_{b,H_2O}) + X_{H_2O,\,a} \quad (9)$$

$$P_{vap,surf} = \frac{\chi_{H_2O,surf} R(T_{surf} + 273.15)}{M_{H_2O}} \quad (10)$$

$$P_{sat}(T_{surf}) = P\exp\left[\frac{M_{H_2O}10^{-3}\gamma}{R}\left(\frac{1}{T_0 + 273.15} - \frac{1}{T_{surf} + 273.15}\right) \times\right] \quad (11)$$

$$RH_{surf} = \frac{P_{vap,surf}}{P_{sat}(T_{surf})} \times 100 \quad (12)$$

where ρ is the air density (kg m^{-3}), C_p is the air specific heat (J kg^{-1} K^{-1}), $\chi_{H_2O,surf}$ and $X_{H_2O,a}$ are the air concentration of water (g m^{-3}) at the surface and reference height, respectively, $X_{H_2O,a}$ is calculated from the air relative humidity, E is the water vapor flux (kg m^{-2} s^{-1}), $P_{vap,surf}$ is the water vapor pressure at the surface (Pa), R is the universal gas constant (J mol^{-1} K^{-1}), M_{H_2O} is the molecular weight of water (g mol^{-1}), $P_{sat}(T_{surf})$ is the saturation vapor pressure at T_{surf} (Pa), P is the atmospheric pressure (Pa), γ is the latent heat of vaporization of water (J kg^{-1}), and T_0 is the boiling temperature of water at P (°C).

2.4 Data quality assurance

The use of the AG method requires some prerequisites, such as stationary but strong enough turbulence, no chemical interference and uniform underlying surface.

First, the AG method under extremely unstable and stagnant conditions were thought to suffer from large uncertainties due to the invalidation of MOST. The ratio of the measurement height and the Obukhov length (z/L) is used to evaluate the atmospheric stability. z/L between −2 and 1 are required. Valid data coverage was 79% with a 30 min time resolution.

Second, the NO titration of ozone, which might cause a substantial surface gradient of ozone, is often regarded as an uncertainty source in ozone flux measurements in some areas.[43] As ozone titration by a considerable NO near the surfaces in agricultural fields could occur in minutes, it might compete with the vertical transport of ozone in determining the surface gradient of ozone. A comparison between the turbulence transport time (τ_{trans}) and the chemical reaction time (τ_{chem}) can be used to evaluate the influence of the chemical reaction on the ozone flux. Following the method of Stella *et al.*,[34] the τ_{trans} can be expressed as the transfer resistance through each layer multiplied by the layer height. The layer height of the quasi-laminar boundary layer, $(z_0 - z_{0'})$, is so small that the contribution of the quasi-laminar boundary to τ_{trans} is negligible. τ_{chem} is calculated as the lifetime of ozone reacting with NO.

$$\tau_{trans} = R_a \times (z_m - z_0) + R_b \times (z_0 - z_{0'}) = R_a \times z_m \quad (13)$$

$$\tau_{chem} = \frac{1}{\chi_{NO}(z_m) \times k_r} \quad (14)$$

where z_m is the measurement height, $\chi_{NO}(z_m)$ is the concentration of NO_PSS (ppbv) at the measurement height. The

reaction rate constant (k_r in ppbv^{-1} s^{-1}) is calculated as $k_r = 0.0444 \times \exp(-1370/(T_a + 273.15))$.[54] NMC site is almost free from interference from anthropogenic emissions due to the extremely low value of NO_PSS with an average of only 58 pptv. τ_{chem} is calculated to be 10-fold that of τ_{trans} (Fig. S1a†), suggesting that this chemical perturbation of the ozone flux measurement is negligible at NMC.

Third, the footprint area of the ozone flux measurement shows *ca.* 3% attribution to the water surface to the west of our measurement site 280 m away (Fig. S1b†). Ozone deposition on the water surface was roughly evaluated based on the turbulence measurement and typical water surface resistance for ozone uptake of 1000 s m^{-1}. The calculated value of v_d is 1/4–1/8 of that on soil. However, considering the contribution of the water surface to the footprint area, corrections of less than 3% for ozone flux measurement are thus abandoned.

The ozone flux is determined from the product of K and $\frac{d[O_3]}{dZ}$ (eqn (1)), thus the uncertainty of ozone flux includes the uncertainty of these two factors, σ_K and $\sigma_{(d[O_3]/dZ)}$. σ_K contains uncertainty from measurements and those arising from the parameterization (eqn (2) and (3)), both of which have larger uncertainty under stable atmospheric conditions, *i.e.* during nighttime. Quantify of σ_K is tough[55] and out of our scope. Constant relative uncertainties of 20% and 50% are given to K, which is robust.[55,56] To validate the estimation of σ_K, we compared H and LE derived separately from the EC method and AG method. It was indicated that the diel profiles were similar, and the magnitudes of H and LE were comparable between the two methods (Fig. S1c and d†). The AG method overestimated H by approximately 10%, and biased LE by a constant systematic error of approximately 18 W m^{-2} compared to the EC method. Further examination of the temperature and moisture gradients suggested that inconsistencies between different hygrothermometers might account for the divergences.

$\sigma_{(d[O_3]/dZ)}$ is determined by the uncertainty of the difference of ozone concentration $\sigma_{\Delta[O_3]}$, because measurement of height is accurate. Ozone concentration at two heights were measured by one ozone analyzer and thus $\sigma_{\Delta[O_3]}$ is equal to $2\sigma_{[O_3]}$, which supposed to be 0.35 ppbv. Whether the ratio $\frac{\Delta[O_3]}{\sigma_{\Delta[O_3]}}$ larger than 1 is used to judge whether $\Delta[O_3]$ is significant. 10% of ozone gradient data were insignificant but still retained to avoid a misestimation of the average flux. It is noteworthy that linear interpolation of the 15 min ozone measurement gaps could be an uncertainty source to the ozone gradient but could not be accurately evaluated. Extreme and unreasonable values of the ozone gradient occasionally appeared from the interpolation method. However, it was plausible to see a typical diel variation of the ozone gradients (Fig. S1e†). Therefore, to reduce the impact of outliers on the analysis, outlier spikes of v_d and maximal or minimal 2.5% of R_{soil} are excluded from the data analysis.

Using Gaussian uncertainty propagation, the uncertainty of ozone flux and ozone deposition velocity could be calculated as follows:

$$\frac{\sigma_F}{F} = \sqrt{\left(\frac{\sigma_K}{K}\right)^2 + \left(\frac{\sigma_{(d[O_3]/dZ)}}{(d[O_3]/dZ)}\right)^2} \approx \sqrt{\left(\frac{\sigma_K}{K}\right)^2 + \left(\frac{\sigma_{\Delta[O_3]}}{\Delta[O_3]}\right)^2} \quad (15)$$

$$\frac{\sigma_{v_d}}{v_d} = \sqrt{\left(\frac{\sigma_F}{F}\right)^2 + \left(\frac{\sigma_{[O_3]}}{[O_3]}\right)^2} \quad (16)$$

$\frac{\sigma_F}{F}$ were dependent on $\frac{\sigma_K}{K}$ during nighttime and dependent on both $\frac{\sigma_K}{K}$ and $\frac{\sigma_{\Delta[O_3]}}{\Delta[O_3]}$ during daytime. Diel $\frac{\sigma_F}{F}$ varies from 25.7% during daytime to 51.1% during nighttime, with an average of 39.8%. As $\frac{\sigma_{[O_3]}}{[O_3]}$ is less than 1%, $\frac{\sigma_{v_d}}{v_d}$ is approximately equal to $\frac{\sigma_F}{F}$.

2.5 Simulation of ozone deposition velocity with different R_{soil} parameterizations

The resistance analogy with the Stella scheme (hereafter called RA_SS) is performed to evaluate the reproducibility of v_d. R_a and R_b are calculated by eqn (6) and (7) with meteorological parameters measured on site. The expression of the Stella scheme is as follows:

$$R_{soil} = R_{soil\ min} \times e^{(k \times RH_{surf})} \quad (17)$$

$$R_{soil\ min} = 702 \times (\text{clay content})^{-0.98} \quad (18)$$

$$k = 0.0118\, e^{0.0266 \times (\text{clay content})} \quad (19)$$

where $R_{soil\ min}$ (s m^{-1}) is the soil resistance when RH_{surf} is 0%, k (unitless) is the coefficient of the exponential function, and clay content (%) is the fraction of clay content in the topsoil. The soil clay content of NMC site, 14.5%, is obtained from the soil dataset by Ito and Wagai.[57]

3 Results and discussion

3.1 Environmental conditions and ozone deposition velocity

The environmental conditions of ozone deposition are largely determined by climate regions. As a typical highland mountain climate region, NMC site features strong solar radiation and cold, arid, and windy meteorological conditions. The measurements covered two periods with distinct meteorological parameters, namely, the premonsoon period before 1 July and the ASM period after 1 July (shaded area in Fig. S2†). In the premonsoon period, solar radiation (R_g) at NMC site was even larger than the solar constant (1367 W m^{-2}) at cloudless noon (Fig. S2a†), with a maximum of 1552.6 W m^{-2} on 11 June. However, with such strong R_g, air temperature (T_a) is quite low due to the buffering effect of plateau permafrost and could be below 0 °C in early May (Fig. S2b†). T_a slowly increased from 4.3 ± 4.3 °C to 11.8 ± 4.0 °C in the premonsoon period. Under the additive effects of low soil water content (SWC) and strong R_g, typical air relative humidity (RH_a) was lower than 25% during the daytime in the premonsoon period (Fig. S2c†). Strong winds occurred frequently, and the wind speed (WS) exceeded 10 m s^{-1} on some days (Fig. S2d†). In the ASM period, the ASM brought abundant moisture to the TP and resulted in more frequent precipitation. R_g showed a dramatic decline compared

to the premonsoon period, but it still remained at a high level compared with regions of the same latitude. Volumetric soil water content (SWC) zoomed from 0.01 to 0.2 after 1 July. Weakened R_g and enhanced SWC in the ASM period caused a slight decrease in T_a and a significant increase in RH_a. WS showed obvious differences from the premonsoon period, with the peak dropping, but WS mean at night increased.

Diel pattern of key parameters that related to calculation of R_a, R_b, R_{soil} and derivation of v_d according to eqn (6)–(12) and (17) are performed in Fig. 2. Over the entire observation period, the hourly mean T_a ranged from 1.6 ± 4.6 °C at night to 10.6 ± 4.3 °C in the daytime (Fig. 2b). Significant enhancements of T_{surf} compared to T_a occurred with a maximal hourly enhancement of 15.6 °C during daytime. This was caused by strong R_g, of which the hourly mean maximal reached 1252.4 ± 348.5 W

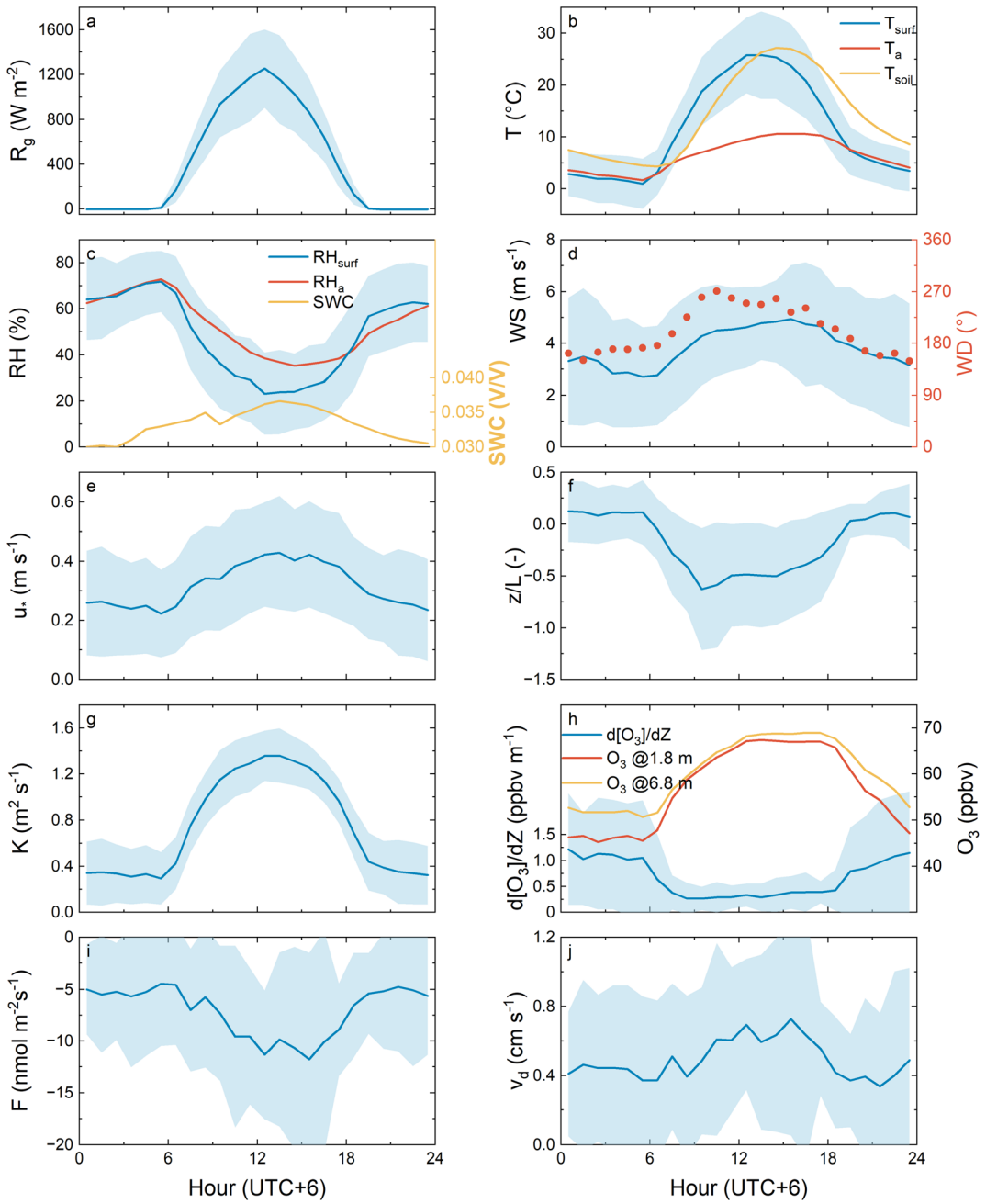

Fig. 2 Diel pattern of meteorological parameters and edaphic parameters associated with ozone deposition velocity derivation and deposition resistance derivation. Diel pattern of (a) solar radiation (R_g), (b) air temperature at 1.8 m (T_a), surface temperature (T_{surf}) and soil temperature at −5 cm (T_{soil}), (c) air relative humidity at 1.8 m (RH_a), surface relative humidity (RH_{surf}) and soil water content (SWC), (d) wind speed at 1.8 m (WS) and wind direction (WD), (e) friction velocity (u_*), (f) atmospheric stability criterion (z/L), (g) turbulence exchange coefficient (K), (h) gradient of ozone between 6.8 m and 1.8 m (d[O_3]/dZ), ozone concentration at 6.8 m and ozone concentration at 1.8 m, (i) ozone flux (F), and (j) ozone deposition velocity (v_d). The solid line is the diel mean, and the shading is variation of our observations.

m^{-2} (Fig. 2a and b). The enhancement of T_{surf} further caused lower RH_{surf} according to eqn (12). RH_{surf} at noon was as low as 23.2 ± 17.8%, which is 15.3% of decrease compared with RH_a (Fig. 2c). The increased T_{surf} and consequently decreased RH_{surf} may result in a small R_{soil}, and thus favors ozone deposition.

Solar radiation and wind supply energy to atmospheric turbulence which affects R_a and R_b. A campaign average R_g of 411.9 ± 469.2 W m^{-2} and wind speed of 3.83 ± 0.72 m s^{-1} (Fig. 2a and d) favored strong atmospheric turbulence. The influence of solar radiation and wind on atmospheric turbulence strength is reflected in the diel pattern of friction velocity (u_*) and z/L (Fig. 2e and f). u_* remained fairly large throughout the day with a maximum of 0.43 ± 0.19 m s^{-1} around noon. The mean u_* during the night dropped to 0.2 m s^{-1}. An opposite diel trend was shown in z/L, with an average of 0.1 at night and −0.5 in the daytime. A nighttime z/L of 0.1 also confirmed that the atmospheric stability at night was nearly neutral and did not seriously block the development of turbulence. Active atmospheric turbulence resulted in rapid vertical turbulence transport, which was characterized by K (eqn (2), (3), and Fig. 2g). The diel pattern of K is similar to those of WS and R_g. Nighttime K remained at approximately 0.3–0.4 m^2 s^{-1}, while K increased to 1.36 ± 0.24 m^2 s^{-1} at noon. It can be inferred from the diel pattern of K and R_g that surface heating driven by solar radiation plays a dominant role in turbulence development at NMC site.

F and v_d are determined based on the K, as well as the measurements of $d[O_3]/dZ$ between 6.8 m and 1.8 m (eqn (1) and (4)). The ozone measured at the two heights showed similar diel profiles but distinct abundances (Fig. 2h). The ozone at 1.8 m ranged from 45.6 ± 11.4 ppbv at night to 67.4 ± 10.4 ppbv in the daytime, with a mean of 56.9 ± 8.6 ppbv. The ozone at 6.8 m ranged from 50.7 ± 12.1 ppbv at night to 69.0 ± 10.3 ppbv in the daytime, with a mean of 60.2 ± 7.0 ppbv. A similar diel profile of F was derived compared to that of K, WS, and R_g (Fig. 2i). Negative values suggested a downward deposition of ozone. The daily mean F was −7.09 ± 2.36 nmol m^2 s^{-1}, with a noontime maximum of −11.78 ± 10.28 nmol m^2 s^{-1}. As the low air pressure counteracts high volume concentrations of ozone to F, the large F could be explained mainly by high v_d. v_d showed a bridge-shaped diel profile (Fig. 2j) with the mean of 0.49 ± 0.11 cm s^{-1} and a noontime peak of 0.73 ± 0.67 cm s^{-1}. The v_d observed here is comparable to typical v_d in forests and one of the highest previously reported over bare soils.[33,58,59] Notably, a high nighttime v_d of approximately 0.4 cm s^{-1} is observed, which is among the top values ever reported.[33] Although nighttime v_d has larger uncertainty than that of daytime, quite high u_* and z/L much less than 1 during nighttime favored high nighttime v_d at NMC.

3.2 Determinative role of R_{soil} in ozone deposition and its variability

The constitution of deposition resistance provides the information to explain the magnitude of v_d and its diel variation. The diel profile of deposition resistance and its components is shown in Fig. 3a. The deposition resistance of ozone, R_{all}, showed a typical U-shaped diel profile, which accounts for the bridge-shaped v_d. Both R_{soil} and $R_a + R_b$ showed a typical U-shaped diel profile as well. The daytime low R_{soil} at NMC site (106.0 ± 22.4 s m^{-1}) was even comparable to the typical daytime R_c over forests (Fig. 3c), which was the lowest resistance due to effective stomatal uptake of ozone by leaves. The nighttime R_{soil}, with a mean of 159.5 ± 30.7 s m^{-1}, was approximately 0.5 times higher than the daytime R_{soil}, but still remained the lowest in literature.[33] Such diel structure of R_{soil} at NMC site was also worthy of highlighting. In comparison, the nighttime R_c on forest canopies was generally 1.5 times (sometimes up to 10 times) higher than the daytime R_c due to the closure of leaf stomata.[27] Mechanism exploration and parameterization of R_{soil} will be discussed in next section. A comparison of daytime $R_a + R_b$ at NMC site (62.3 ± 15.8 s m^{-1}) with previous studies in various environments (56.5 ± 25.7 s m^{-1}) indicated efficient atmospheric turbulent transport at NMC site (Fig. 3b). A much smaller nighttime $R_a + R_b$ here (110.4 ± 15.3 s m^{-1} *vs.* 200.5 ± 101.0 s m^{-1} in various environments) implied the more rapid ozone deposition at night as well. $R_a + R_b$ is reasonably well defined and can be expressed by a function of u_* and z/L (eqn (6) and (7)), which are affected by WS and R_g. Strong WS and R_g at NMC site allow neither a high $R_a + R_b$ nor a very low $R_a + R_b$ due to the insensitive response of $R_a + R_b$ to WS at its high value end.

Similar to previous impressions, R_{soil} is the major fraction (62 ± 7%) of R_{all} during both the daytime and the nighttime, suggesting R_{soil} plays the dominant role in ozone deposition at NMC site. The low R_{soil} and $R_a + R_b$ together explain large v_d in both daytime and nighttime. The spatial variability in R_{soil} and v_d over different climates across 3 orders of magnitude (Fig. 3c and S3†), whereas the span range of R_{soil} at NMC site is the smallest and distributed at the lower end of reported R_{soil}. To date, our study reported the only observation of R_{soil} in highland climate regions, and the significant differences from previous studies highlighted the heterogeneity of R_{soil} over different climates.

3.3 Variability of R_{soil} and its parameterization

In-depth understanding of soil uptake of ozone could help to establish a more robust empirical parameterization of R_{soil}. Clifton *et al.*[27] proposed a mechanistic model of R_{soil}, which represents ozone reaction with soil surfaces and gases in soil pore spaces. Although it is tough to measure all of the parameters required for the mechanistic model in a field observation, it provides a roadmap to identify key parameters that control R_{soil}. Both the mechanistic model and previous observations[34–37] have found that moisture and temperature are two key parameters that control the temporal variability of R_{soil}.

Moisture is suggested a major influencing factor of R_{soil} based on both mechanical deduction and observations.[27,34,37] The inhibition of soil ozone uptake by moisture is reflected in two ways.[34] First, soil moisture can block the diffusion of ozone in soil. Second, water molecules can be adsorbed by soil and occupy the reactive surface site, thus competing with ozone absorption and reactive uptake. The

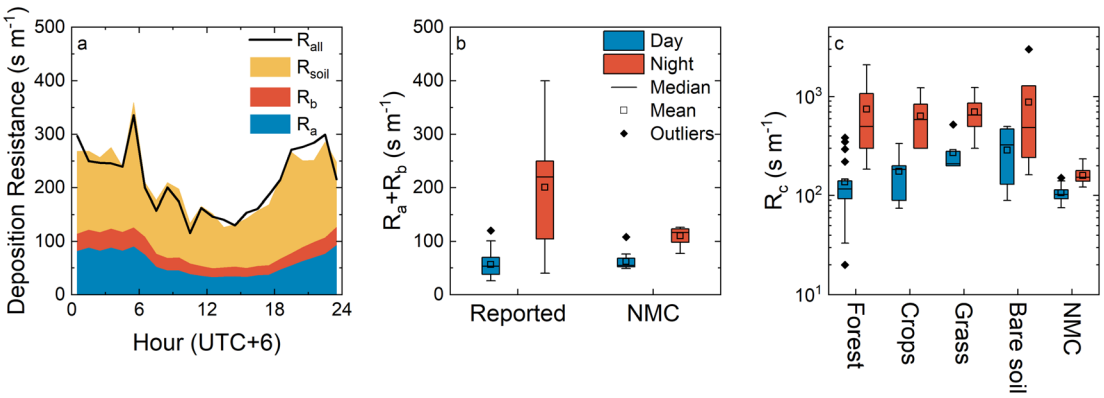

Fig. 3 (a) Median diel pattern of deposition resistance of observation at NMC site. Hourly medians are utilized instead of hourly means due to the skewed distribution of R_{all} and R_{soil}. (b) Comparison of R_a + R_b and reported R_a + R_b during day and night. (c) Comparison of observed R_{soil} and reported R_c over different conditions during day and night. Parts of reported R_c are obtained by $1/v_d$ minus prescribed R_a + R_b (50 s m^{-1} during daytime and 200 s m^{-1} during nighttime). Data from.[24,26,58–67]

two mechanisms account for a positive dependence of R_{soil} on moisture as widely observed in field observations and laboratory experiments.[27] Our observation at NMC site also showed a significant positive dependence of R_{soil} on RH_{surf} (Fig. 4a). The dry climate at NMC site is conducive to keeping R_{soil} small.

Temperature is a positive-going parameter for ozone uptake, as the reaction of ozone on the surface is endothermic. Thus, R_{soil} decreases with increasing temperature. The mechanical deduction requires an Arrhenius-like response of R_{soil} to temperature, which is verified in field observations but with large fitting uncertainty and variability.[34–36] The negative relationship between R_{soil} and temperature was also observed at NMC site (Fig. 4b). Notably, the dependence of R_{soil} on temperature could be a misconception due to the highly negative correlation between temperature and moisture. As a result, it is difficult to distinguish the individual effect of temperature from RH_{surf} on R_{soil}. Nevertheless, high T_{surf} is conducive to lower R_{soil}.

As shown in Fig. 5a and b, R_{soil} can be described by an exponential equation of RH_{surf} and an Arrhenius-like function of T_{surf} (eqn (20) and (21)):

$$R_{soil} = 71.0 \times e^{0.012 \times RH_{surf}} \quad (20)$$

$$R_{soil} = 0.52 \times e^{\frac{12850}{RT_{surf}}} \quad (21)$$

These two parameterization schemes were tested by simulating v_d with observation-constrained meteorological data by employing eqn (5)–(7) (Fig. 5c). Similar results of v_d are obtained from the two parameterization schemes and both results are closely comparable to the observed v_d in terms of both the magnitude and the temporal variability. Stella *et al.*[34] have found that the parameterization scheme with RH_{surf} performed more robustly than the parameterization scheme with T_{surf}. A potential reason for this could be that RH_{surf} itself contains the influence of T_{surf} due to the high correlation between RH_{surf} and T_{surf}, as previously mentioned. Herein, we choose the

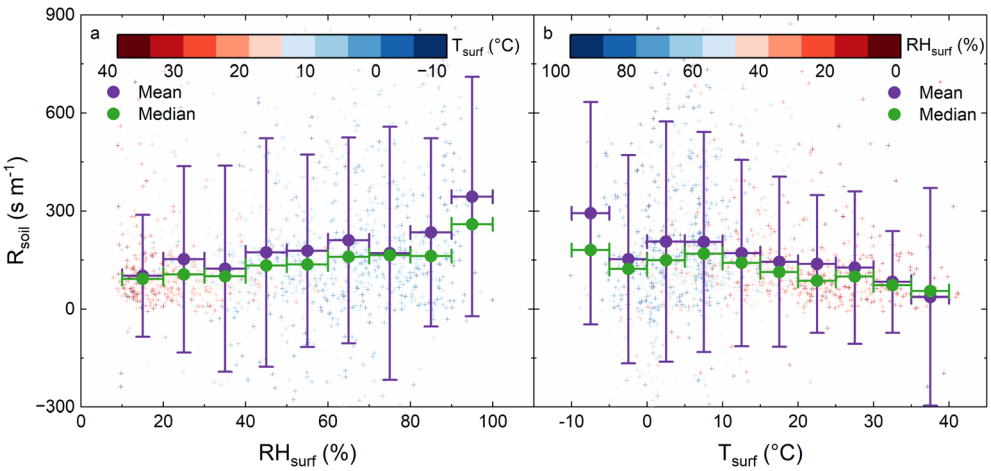

Fig. 4 Dependence of R_{soil} on (a) RH_{surf} and (b) T_{surf}. The block processing ranges of means and medians of RH_{surf} and T_{surf} are 10% and 5 °C, respectively.

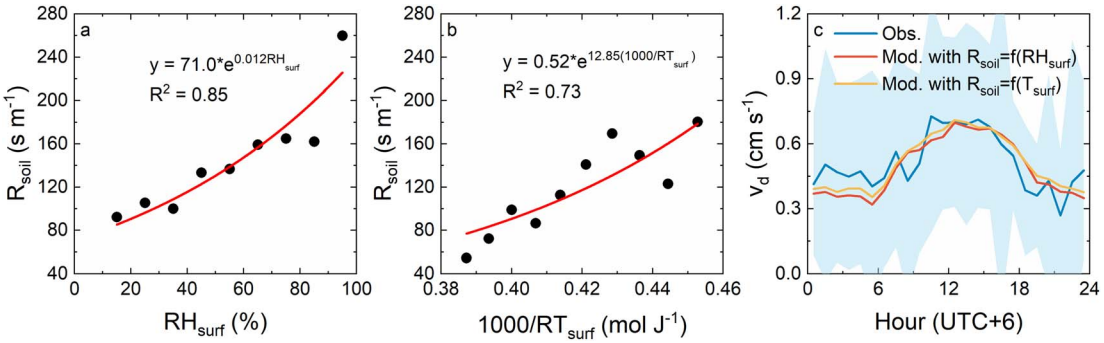

Fig. 5 R_{soil} as a function of (a) RH_{surf} and (b) T_{surf}. Dots are block median data with ranges of 10% for RH_{surf} and 5 °C for T_{surf}. (c) Comparison of observed v_d and simulated v_d using R_{soil} as a function of RH_{surf} and T_{surf} with input meteorological data from observations. The shading area for observation represents 1 sd of observed v_d. Time alignments are performed on the data used for comparison.

parameterization scheme with RH_{surf} for further discussion. According to eqn (20), R_{soil} is predicted to be lower than 240 s m^{-1} at NMC site even at a high RH_{surf} range, which explains the rapid ozone deposition at night. In addition, strong solar radiation and dry conditions during the daytime maintain high T_{surf} and low RH_{surf}, which are also conducive to low R_{soil}.

Block medians instead of block means of R_{soil} were chosen to fit the function among R_{soil} and RH_{surf} (or T_{surf}) in this study, since R_{soil} at NMC was positively skewed. The fitting function based on block medians turned out to better reproduce our observations than that based on block means (Fig. 5 and S4†). As a matter of fact, R_{soil} is consistently found to be positively skewed.[26,65,67,68] Thus, it needs more attention about whether the function among R_{soil} and RH_{surf} (or T_{surf}) are fitted with block medians or block means. Block means of R_{soil} were used in the establishment of the Stella scheme,[33,34] which should be further examined.

3.4 Evaluation and improvement of the Stella scheme

RH_{surf} explains the variability of R_{soil} at specific sites, while soil clay content determines the site-by-site variability by affecting $R_{soil\ min}$ and k. According to the fitted results in eqn (20), $R_{soil\ min}$ and k of NMC are 71.0 s m^{-1} and 0.012, respectively. We applied the Stella scheme reversely (eqn (17)–(19)) and derived $R_{soil\ min}$ = 51.0 s m^{-1} and k = 0.017 at NMC. Compared with the observed $R_{soil\ min}$ (71.0 s m^{-1}) and k (0.012), the Stella scheme underestimated $R_{soil\ min}$ by 28% and overestimated k by 42% (red dots in Fig. 6a and b). By including our observations on $R_{soil\ min}$ and k, we updated the Stella scheme (hereafter called the updated Stella scheme, eqn (17), (20) and (21). To be noted, observations at La Crau were not included fitting in both the Stella scheme and the updated Stella scheme due to the reason mentioned in Stella *et al.*,[33] where the reported soil clay content is not representative.

$$R_{soil\ min} = 661 \times (\text{clay content})^{-0.86} \quad (22)$$

$$k = 0.0093\, e^{0.0325\times(\text{clay content})} \quad (23)$$

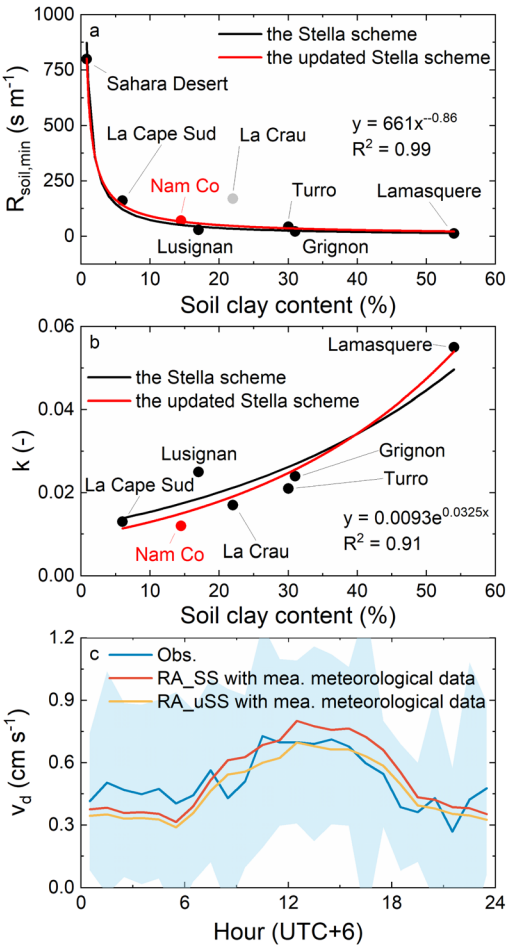

Fig. 6 Relationships between soil clay content and two coefficients in the Stella scheme, (a) minimum soil resistance ($R_{soil\ min}$) and (b) k. The black dots are values collected from previous observations, and the red dots are values from our observation at NMC site. The Stella scheme are shown as black lines, and the updated Stella scheme are shown as red lines. (c) Comparison of observed v_d and simulated v_d using the RA_SS and resistance analogy with the updated Stella scheme (RA_uSS) with input meteorological data from observations. Time alignments are performed on the data used for comparison.

The updated Stella scheme of course improved the scheme representation of R_{soil} at NMC, relative to the Stella scheme. The simulation error of $R_{soil\ min}$ and k was reduced from 28% and 42% to 7% and 25%. A better representative R_{soil} led to a better representation of v_d (Fig. 6c). The resistance analogy with the updated Stella scheme (RA_uSS) reproduced the observed daytime mean of v_d of 0.58 cm s^{-1}. Almost the same diel pattern of v_d was modelled by the RA_SS and overestimated daytime v_d by only 14%. Our observations validate the feasibility of the Stella scheme and illustrate the need to include more observations in the Stella scheme.

The above analysis suggests that v_d is sensitive to both $R_{soil\ min}$ and k. Assuming ±25% spread in $R_{soil\ min}$ and k, the spread in daytime and nighttime v_d are calculated by the RA_uSS with typical RH_{surf} (40% during daytime and 80% during nighttime) and $R_a + R_b$ (50 s m^{-1} during daytime and 200 s m^{-1} during nighttime). v_d generally varied in a narrow range responding to $R_{soil\ min}$ changes across the entire soil clay content range (Fig. 7a). The sensitivity of v_d to k increases exponentially with increasing clay content (Fig. 7b). In the high soil clay content range, the ±25% spread in k could cause more than 200% change in v_d. The sensitivity of v_d to k also increases with RH_{surf}. As a result, nighttime v_d is more sensitive than daytime v_d for a much higher RH_{surf} range over the night. Therefore, observation verification on high soil clay contents and high RH_{surf} are especially useful, though all observation verifications on varied climatic environments worthy to be highlighted, for the sake of continuous test and improvement of the updated Stella scheme.

3.5 Implications of the updated Stella scheme

The updated Stella scheme provides a comprehensive view of the distributions of R_{soil} and v_d over soil in various soil and hydrothermal conditions (Fig. 8). The rough range of soil clay content and hydrothermal conditions in different climates are also performed in Fig. 8a and b. A commonly used R_{soil} in CTMs (black solid line in Fig. 8a) overestimates R_{soil} in most climate regions and thus causes the underestimation of v_d over soil (black solid line in Fig. 8b). And the great variability of R_{soil} and v_d over soil among different climate regions are not reproduced.

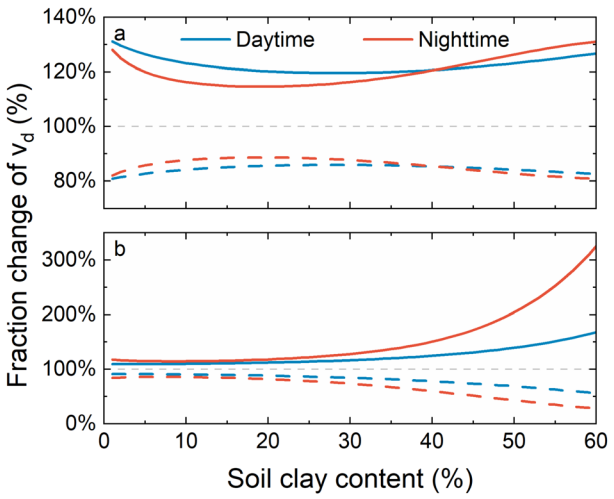

Fig. 7 Sensitivity test of daytime and nighttime v_d responding to a ±25% spread (−25% and +25% change are shown in solid lines and dash lines, respectively) in (a) $R_{soil\ min}$ or (b) k as calculated by the updated Stella scheme with typical RH_{surf} (40% during daytime and 80% during nighttime) and $R_a + R_b$ (50 s m^{-1} during daytime and 200 s m^{-1} during nighttime).

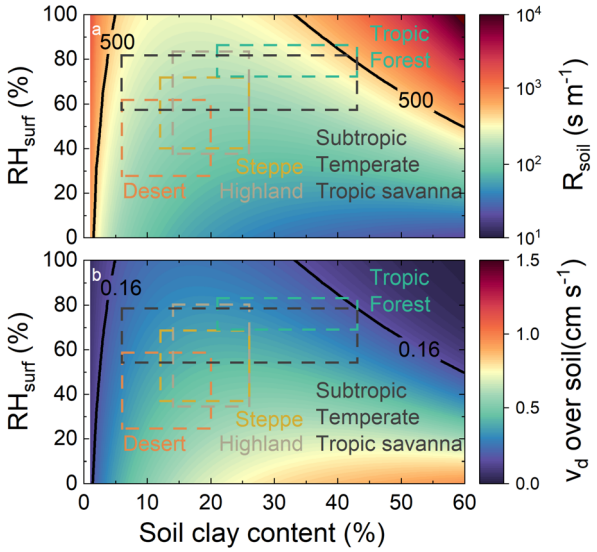

Fig. 8 Dependence of R_{soil} and v_d over soil on soil clay content and hydrothermal conditions. Theoretical distribution of (a) R_{soil} and (b) v_d over soil with different soil clay contents and RH_{surf}. R_{soil} is calculated with the updated Stella scheme. v_d is the mean of daytime and nighttime v_d. The daytime and nighttime v_d are calculated with the assumed $R_a + R_b$ (50 s m^{-1} during the daytime and 200 s m^{-1} during the nighttime) and calculated R_{soil}. The solid black line in (a) represents a commonly used R_{soil} in CTMs (500 s m^{-1}) and in (b) represents the v_d calculated with R_{soil} = 500 s m^{-1}. Data of climate classification and soil clay content are the same with Fig. 1. The HadISDH data[69,70] is used to estimate the approximate RH_{surf} ranges of different climates.

The delineation of different climate regions in Fig. 8 is helpful to establish a general impression of the distribution of R_{soil} and v_d over soil in real environments. In desert, coarse soil could cause high $R_{soil\ min}$ and R_{soil}, and thus low v_d. As for tropical forest climate regions, high RH_{surf} causes extremely high R_{soil} and low v_d over soil, thus deposition on canopy would be the major path. In vast areas of other climates, moderate soil clay content and RH_{surf} supply low R_{soil} and therefore high v_d over soil, especially in highland climate regions and steppe. Our observation in fact provides the confirmation of high v_d over soil in highland climate regions. Stella *et al.*[33] provides five observations in the subtropical climate region. More observations in different climate regions, especially in desert, steppe, and highland are needed to evaluate and improve the Stella scheme or the updated Stella scheme.

4 Conclusions and perspectives

This study reported the first measurement of ozone deposition in a typical highland background site with bare soil in the central TP. Unexpectedly high v_d with a daily mean of 0.49 ± 0.11 cm s^{-1} and an hourly mean maximum of 0.73 ± 0.67 cm s^{-1} was found.

Strong solar radiation and high wind speed provided efficient turbulence energy, especially in the daytime, suggesting that atmospheric transports to the surface were not limiting steps most of the time. The soil uptake process was the main controlling process of ozone deposition at NMC. Soil uptake rate, as well as $1/R_{soil}$, was found among the top in the literature. Such high $1/R_{soil}$ was regulated by proper soil clay content, dry conditions, and strong solar radiation in the TP. These favorable conditions of soil ozone deposition are common in the TP and other highland regions. Therefore, ozone deposition in the TP and highland regions was validated as being underestimated by current models.

The Stella scheme is proven to be an effective parameterization of R_{soil} by our verification at NMC site. The Stella scheme was updated through the inclusion of our observations and then better represented R_{soil} and thus v_d at NMC. The updated Stella scheme is recommended as a replacement for the prescribed values of R_{soil} in current CTMs. Notably, both the Stella scheme and the updated Stella scheme showed the potential for continuous improvement. More quality and representative field observations of R_{soil} are encouraged to further minimize the fitting uncertainty of $R_{soil\ min}$ and k in the Stella scheme. Observation verifications that meet the following requirements will be helpful. First, soil deposition should be isolated from other paths of ozone deposition, such as observations over bare soils or chambers in the ground. Second, to avoid interference of reactive gases, pristine bare soils or inactivated soils are recommended. Third, perform measurements under different climatic environments to obtain different combinations of soil clay content and hydrothermal conditions. Finally, long-term and even year-round observations should be conducted to obtain a wider range of variations in the combination of RH_{surf} and T_{surf}.

Author contributions

Chong Zhang: data curation, formal analysis, investigation, methodology, software, visualization, writing – original draft, writing – review & editing; Jianshu Wang: investigation, writing – review & editing; Yingjie Zhang: conceptualization, funding acquisition, investigation, methodology, project administration, writing – review & editing; Wanyun Xu: data curation, investigation, writing – review & editing; Gen Zhang: investigation, writing – review & editing; Guofang Miao: software, writing – review & editing; Jiacheng Zhou: investigation, writing – review & editing; Hui Yu: investigation, writing – review & editing; Weixiong Zhao: writing – review & editing; Weili Lin: writing – review & editing; Ling Kang: resources, writing – review & editing; Xuhui Cai: writing – review & editing; Hongsheng Zhang: writing – review & editing; Chunxiang Ye: conceptualization, funding acquisition, investigation, methodology, project administration, resources, supervision, writing – review & editing.

Conflicts of interest

There are no conflicts to declare.

Acknowledgements

This work was supported by the Second Tibetan Plateau Scientific Expedition and Research Program (2019QZKK060604) and the National Natural Science Foundation of China (grants no. 42105110).The authors acknowledge all researchers involved in the @Tibet 2019 campaign. Thanks for the support from the Nam Co Comprehensive Observation and Research Station of Chinese Academy of Sciences.

References

1 E. A. Ainsworth, C. R. Yendrek, S. Sitch, W. J. Collins and L. D. Emberson, *Annu. Rev. Plant Biol.*, 2012, **63**, 637–661.
2 T.-M. Fu and H. Tian, *Curr. Pollut. Rep.*, 2019, **5**, 159–171.
3 N. E. Grulke and R. L. Heath, *Plant Biol.*, 2020, **22**, 12–37.
4 M. Jerrett, R. T. Burnett, C. Arden Pope, K. Ito, G. Thurston, D. Krewski, Y. Shi, E. Calle and M. Thun, *N. Engl. J. Med.*, 2009, **360**, 1085–1095.
5 M. G. Schultz, S. Schröder, O. Lyapina, O. R. Cooper, I. Galbally, I. Petropavlovskikh, E. von Schneidemesser, H. Tanimoto, Y. Elshorbany, M. Naja, R. J. Seguel, U. Dauert, P. Eckhardt, S. Feigenspan, M. Fiebig, A.-G. Hjellbrekke, Y.-D. Hong, P. C. Kjeld, H. Koide, G. Lear, D. Tarasick, M. Ueno, M. Wallasch, D. Baumgardner, M.-T. Chuang, R. Gillett, M. Lee, S. Molloy, R. Moolla, T. Wang, K. Sharps, J. A. Adame, G. Ancellet, F. Apadula, P. Artaxo, M. E. Barlasina, M. Bogucka, P. Bonasoni, L. Chang, A. Colomb, E. Cuevas-Agulló, M. Cupeiro, A. Degorska, A. Ding, M. Fröhlich, M. Frolova, H. Gadhavi, F. Gheusi, S. Gilge, M. Y. Gonzalez, V. Gros, S. H. Hamad, D. Helmig, D. Henriques, O. Hermansen, R. Holla, J. Hueber, U. Im, D. A. Jaffe, N. Komala, D. Kubistin, K.-S. Lam, T. Laurila, H. Lee, I. Levy, C. Mazzoleni, L. R. Mazzoleni, A. McClure-Begley, M. Mohamad, M. Murovec, M. Navarro-Comas, F. Nicodim, D. Parrish, K. A. Read, N. Reid, L. Ries, P. Saxena, J. J. Schwab, Y. Scorgie, I. Senik, P. Simmonds, V. Sinha, A. I. Skorokhod, G. Spain, W. Spangl, R. Spoor, S. R. Springston, K. Steer, M. Steinbacher, E. Suharguniyawan, P. Torre, T. Trickl, L. Weili, R. Weller, X. Xiaobin, L. Xue and M. Zhiqiang, *Elem. Sci. Anth.*, 2017, **5**, 58.
6 A. T. Archibald, J. L. Neu, Y. F. Elshorbany, O. R. Cooper, P. J. Young, H. Akiyoshi, R. A. Cox, M. Coyle, R. G. Derwent, M. Deushi, A. Finco, G. J. Frost, I. E. Galbally, G. Gerosa, C. Granier, P. T. Griffiths, R. Hossaini, L. Hu, P. Jöckel, B. Josse, M. Y. Lin, M. Mertens, O. Morgenstern, M. Naja, V. Naik, S. Oltmans, D. A. Plummer, L. E. Revell, A. Saiz-Lopez, P. Saxena, Y. M. Shin, I. Shahid, D. Shallcross, S. Tilmes, T. Trickl, T. J. Wallington, T. Wang, H. M. Worden and G. Zeng, *Elementa*, 2020, **8**, 1–53.
7 O. E. Clifton, F. Paulot, A. M. Fiore, L. W. Horowitz, G. Correa, C. B. Baublitz, S. Fares, I. Goded, A. H. Goldstein, C. Gruening, A. J. Hogg, B. Loubet, I. Mammarella, J. W. Munger, L. Neil, P. Stella, J. Uddling,

T. Vesala and E. Weng, *J. Geophys. Res.: Atmos.*, 2020, **125**, e2020JD032398.
8 A. Y. H. Wong, J. A. Geddes, A. P. K. Tai and S. J. Silva, *Atmos. Chem. Phys.*, 2019, **19**, 14365–14385.
9 D. Simpson, *Atmos. Environ., Part A*, 1992, **26**, 1609–1634.
10 J.-T. Lin, D. Youn, X.-Z. Liang and D. J. Wuebbles, *Atmos. Environ.*, 2008, **42**, 8470–8483.
11 S. Solberg, Ø. Hov, A. Søvde, I. S. A. Isaksen, P. Coddeville, H. De Backer, C. Forster, Y. Orsolini and K. Uhse, *J. Geophys. Res.: Atmos.*, 2008, **113**(D7), DOI: 10.1029/2007JD009098.
12 M. L. Wesely, *Atmos. Environ.*, 1989, **23**, 1293–1304.
13 T. Emmerichs, A. Kerkweg, H. Ouwersloot, S. Fares, I. Mammarella and D. Taraborrelli, *Geosci. Model Dev.*, 2021, **14**, 495–519.
14 S. Falk and A. Søvde Haslerud, *Geosci. Model Dev.*, 2019, **12**, 4705–4728.
15 I. Lagzi, R. Mészáros, L. Horváth, A. Tomlin, T. Weidinger, T. Turányi, F. Ács and L. Haszpra, *Atmos. Environ.*, 2004, **38**, 6211–6222.
16 R. J. Park, S. K. Hong, H.-A. Kwon, S. Kim, A. Guenther, J.-H. Woo and C. P. Loughner, *Atmos. Chem. Phys.*, 2014, **14**, 7929–7940.
17 L. Zhang, J. R. Brook and R. Vet, *Atmos. Chem. Phys.*, 2003, **3**, 2067–2082.
18 S. Galmarini, P. Makar, O. E. Clifton, C. Hogrefe, J. O. Bash, R. Bellasio, R. Bianconi, J. Bieser, T. Butler, J. Ducker, J. Flemming, A. Hodzic, C. D. Holmes, I. Kioutsioukis, R. Kranenburg, A. Lupascu, J. L. Perez-Camanyo, J. Pleim, Y.-H. Ryu, R. San Jose, D. Schwede, S. Silva and R. Wolke, *Atmos. Chem. Phys.*, 2021, **21**, 15663–15697.
19 Z. Wu, D. B. Schwede, R. Vet, J. T. Walker, M. Shaw, R. Staebler and L. Zhang, *J. Adv. Model. Earth Syst.*, 2018, **10**, 1571–1586.
20 D. Schwede, L. Zhang, R. Vet and G. Lear, *Atmos. Environ.*, 2011, **45**, 1337–1346.
21 E. Lamaud, A. Carrara, Y. Brunet, A. Lopez and A. Druilhet, *Atmos. Environ.*, 2002, **36**, 77–88.
22 K. F. Zeller and N. T. Nikolov, *Environ. Pollut.*, 2000, **107**, 1–20.
23 S. Fares, F. Savi, J. Muller, G. Matteucci and E. Paoletti, *Agric. For. Meteorol.*, 2014, **198–199**, 181–191.
24 K. Matsuda, I. Watanabe, V. Wingpud, P. Theramongkol, P. Khummongkol, S. Wangwongwatana and T. Totsuka, *Atmos. Environ.*, 2005, **39**, 2571–2577.
25 A. J. Visser, L. N. Ganzeveld, I. Goded, M. C. Krol, I. Mammarella, G. Manca and K. F. Boersma, *Atmos. Chem. Phys.*, 2021, **21**, 18393–18411.
26 M. Coyle, E. Nemitz, R. Storeton-West, D. Fowler and J. N. Cape, *Agric. For. Meteorol.*, 2009, **149**, 655–666.
27 O. E. Clifton, A. M. Fiore, W. J. Massman, C. B. Baublitz, M. Coyle, L. Emberson, S. Fares, D. K. Farmer, P. Gentine, G. Gerosa, A. B. Guenther, D. Helmig, D. L. Lombardozzi, J. W. Munger, E. G. Patton, S. E. Pusede, D. B. Schwede, S. J. Silva, M. Sörgel, A. L. Steiner and A. P. K. Tai, *Rev. Geophys.*, 2020, **58**, e2019RG000670.
28 L. Horváth, P. Koncz, A. Móring, Z. Nagy, K. Pintér and T. Weidinger, *Bound. -Layer Meteorol.*, 2017, **167**, 303–326.
29 P. Stella, E. Personne, E. Lamaud, B. Loubet, I. Trebs and P. Cellier, *J. Geophys. Res.: Biogeosci.*, 2013, **118**, 1120–1132.
30 E. Lamaud, B. Loubet, M. Irvine, P. Stella, E. Personne and P. Cellier, *Agric. For. Meteorol.*, 2009, **149**, 1385–1396.
31 S. J. Silva and C. L. Heald, *J. Geophys. Res.: Atmos.*, 2018, **123**, 559–573.
32 P. Stella, E. Personne, B. Loubet, E. Lamaud, E. Ceschia, P. Béziat, J. M. Bonnefond, M. Irvine, P. Keravec, N. Mascher and P. Cellier, *Biogeosciences*, 2011, **8**, 2869–2886.
33 P. Stella, B. Loubet, C. de Berranger, X. Charrier, E. Ceschia, G. Gerosa, A. Finco, E. Lamaud, D. Serça, C. George and R. Ciuraru, *Atmos. Environ.*, 2019, **199**, 202–209.
34 P. Stella, B. Loubet, E. Lamaud, P. Laville and P. Cellier, *Agric. For. Meteorol.*, 2011, **151**, 669–681.
35 J. N. Cape, R. Hamilton and M. R. Heal, *Atmos. Environ.*, 2009, **43**, 1116–1123.
36 I. Fumagalli, C. Gruening, R. Marzuoli, S. Cieslik and G. Gerosa, *Agric. For. Meteorol.*, 2016, **228–229**, 205–216.
37 W. J. Massman, *Atmos. Environ.*, 2004, **38**, 2323–2337.
38 S. Bassin, P. Calanca, T. Weidinger, G. Gerosa and J. Fuhrer, *Atmos. Environ.*, 2004, **38**, 2349–2359.
39 D. Chen and H. W. Chen, *Environ. Dev.*, 2013, **6**, 69–79.
40 FAO and IIASA, *Harmonized World Soil Database version 2.0*, 2023.
41 M. Kummu, M. Heino, M. Taka, O. Varis and D. Viviroli, *One Earth*, 2021, **4**, 720–729.
42 P. Stella, B. Loubet, P. Laville, E. Lamaud, M. Cazaunau, S. Laufs, F. Bernard, B. Grosselin, N. Mascher, R. Kurtenbach, A. Mellouki, J. Kleffmann and P. Cellier, *Atmos. Meas. Tech.*, 2012, **5**, 1241–1257.
43 R. M. Vuolo, B. Loubet, N. Mascher, J. C. Gueudet, B. Durand, P. Laville, O. Zurfluh, R. Ciuraru, P. Stella and I. Trebs, *Biogeosciences*, 2017, **14**, 2225–2244.
44 J. Wang, Y. Zhang, C. Zhang, Y. Wang, J. Zhou, L. K. Whalley, E. J. Slater, J. E. Dyson, W. Xu, P. Cheng, B. Han, L. Wang, X. Yu, Y. Wang, R. Woodward-Massey, W. Lin, W. Zhao, L. Zeng, Z. Ma, D. E. Heard and C. Ye, *Environ. Sci. Technol.*, 2023, **57**, 5474–5484.
45 X. Xu, H. Zhang, W. Lin, Y. Wang, W. Xu and S. Jia, *Atmos. Chem. Phys.*, 2018, **18**, 5199–5217.
46 X. Yin, S. Kang, B. de Foy, Z. Cong, J. Luo, L. Zhang, Y. Ma, G. Zhang, D. Rupakheti and Q. Zhang, *Atmos. Chem. Phys.*, 2017, **17**, 11293–11311.
47 W. Lin, X. Xu, X. Zheng, J. Dawa, C. Baima and J. Ma, *J. Environ. Sci.*, 2015, **31**, 133–145.
48 J. Huang, S. Kang, Q. Zhang, H. Yan, J. Guo, M. G. Jenkins, G. Zhang and K. Wang, *Atmos. Environ.*, 2012, **62**, 540–550.
49 L. Wang, C. Yi, X. Xu, B. Schütt, K. Liu and L. Zhou, *J. Mt. Sci.*, 2009, **6**, 354–361.
50 B. Fang, W. Zhao, X. Xu, J. Zhou, X. Ma, S. Wang, W. Zhang, D. S. Venables and W. Chen, *Opt. Express*, 2017, **25**, 26910.
51 Z. Y. Wu, L. Zhang, X. M. Wang and J. W. Munger, *Atmos. Chem. Phys.*, 2015, **15**, 7487–7496.

52 M. Mauder, M. Cuntz, C. Drüe, A. Graf, C. Rebmann, H. P. Schmid, M. Schmidt and R. Steinbrecher, *Agric. For. Meteorol.*, 2013, **169**, 122–135.
53 N. Kljun, P. Calanca, M. W. Rotach and H. P. Schmid, *Bound. -Layer Meteorol.*, 2004, **112**, 503–523.
54 S. Walton, M. W. Gallagher and J. H. Duyzer, *Atmos. Environ.*, 1997, **31**, 2915–2931.
55 V. Wolff, I. Trebs, T. Foken and F. X. Meixner, *Biogeosciences*, 2010, **7**, 1729–1744.
56 J. Rinne, J.-P. Tuovinen, T. Laurila, H. Hakola, M. Aurela and H. Hypén, *Agric. For. Meteorol.*, 2000, **102**, 25–37.
57 A. Ito and R. Wagai, *Sci. Data*, 2017, **4**, 170103.
58 S. Cieslik, *Environ. Pollut.*, 2009, **157**, 1487–1496.
59 R. Wada, S. Yonemura, A. Tani and M. Kajino, *J. Agric. Meteorol.*, 2023, **79**, 38–48.
60 D. Fowler, C. Flechard, J. N. Cape, R. L. Storeton-West and M. Coyle, *Water, Air, Soil Pollut.*, 2001, **130**, 63–74.
61 G. Gerosa, R. Marzuoli, S. Cieslik and A. Ballarin-Denti, *Atmos. Environ.*, 2004, **38**, 2421–2432.
62 T. P. Meyers, P. Finkelstein, J. Clarke, T. G. Ellestad and P. F. Sims, *J. Geophys. Res.: Atmos.*, 1998, **103**, 22645–22661.
63 M. Michou, P. Laville, D. Serça, A. Fotiadi and V.-H. Peuch, *Atmos. Res.*, 2005, **74**, 89–116.
64 T. N. Mikkelsen, H. Ro-Poulsen, M. F. Hovmand, N. O. Jensen, K. Pilegaard and A. H. Egeløv, *Atmos. Environ.*, 2004, **38**, 2361–2371.
65 C. A. Pio, M. S. Feliciano, A. T. Vermeulen and E. C. Sousa, *Atmos. Environ.*, 2000, **34**, 195–205.
66 M. Zapletal, P. Cudlín, P. Chroust, O. Urban, R. Pokorný, M. Edwards-Jonášová, R. Czerný, D. Janouš, K. Taufarová, Z. Večeřa, P. Mikuška and E. Paoletti, *Environ. Pollut.*, 2011, **159**, 1024–1034.
67 L. Zhang, J. R. Brook and R. Vet, *Atmos. Environ.*, 2002, **36**, 4787–4799.
68 L. Zhang, M. D. Moran, P. A. Makar, J. R. Brook and S. Gong, *Atmos. Environ.*, 2002, **36**, 537–560.
69 K. M. Willett, R. J. H. Dunn, P. W. Thorne, S. Bell, M. de Podesta, D. E. Parker, P. D. Jones and C. N. Williams Jr, *Clim. Past*, 2014, **10**, 1983–2006.
70 A. Smith, N. Lott and R. Vose, *Bull. Am. Meteorol. Soc.*, 2011, **92**, 704–708.